A High-Gain MIMO Lens Antenna with Meta-Transmissive Surface for Dual Circular Polarization Conversion in 6G Terrestrial, Airborne, and Non-Terrestrial Communication Networks

Muhammad Hussain
Photonic/Wireless Devices Research
Division
Electronics and Telecommunication
Research Institute (ETRI)
34129, Daejeon, South Korea
muhammad.hussain@etri.re.kr

Jaeseong Kim
Photonic/Wireless Devices Research
Division
Electronics and Telecommunication
Research Institute (ETRI)
34129, Daejeon, South Korea
kjs63111@etri.re.kr

Hyunjong Choi

Department of Computer Science

Korea University

02841, Seoul, South Korea

wanky95@korea.ac.kr

Minhyup Song
Photonic/Wireless Devices Research
Division
Electronics and Telecommunication
Research Institute (ETRI)
34129, Daejeon, South Korea
sminhyup@etri.re.kr

Abstract— The proposed Multi-Input Multi-Output lens antenna (MIMO-LA), integrated with a dual circularly polarized meta-transmissive surface (DCP-MTS), enhances the realized gain and aperture efficiency by effectively addressing key MIMO performance metrics, including diversity gain (DG), envelope correlation coefficient (ECC), mean effective gain (MEG), and multiplexing efficiency (Mx. Eff.). By incorporating an extended transition and reflective wall along with DCP-MTS, the MIMO-LA achieves a realized gain of 13.58 dBi, a DG of 10 dB, an ECC of 0.01, a MEG of -3 dB, Mx. Eff. of -3.02 dB, while maintaining an aperture efficiency of 50.8 % at the operating frequency $f_0 = 7$ GHz. These results validate the effectiveness of the proposed design for 6G industrial applications, particularly in terrestrial, airborne, and non-terrestrial communications networks.

Keywords— artificial magnetic conductors (AMC), aperture efficiency, diversity gain (DG), envelope correlation coefficient (ECC), Multi-Input Multi-Output lens antenna (MIMO-LA), meta-transmissive surface (MTS), mean effective gain (MEG), multiplexing efficiency (Mx. Eff.), peak realized gain

I. INTRODUCTION

The evolution toward sixth-generation (6G) wireless communication [1, 2] demands innovative antenna solutions [3, 4] capable of delivering high gain, broad bandwidth, and robust polarization diversity across various platforms, including terrestrial [5, 6], airborne [7], and non-terrestrial communication networks [8, 9]. These emerging scenarios impose stringent requirements on antenna, demanding features varying refractive index distributions [10-14], high performance for reliable connectivity, enhanced spectral efficiency, and minimal interference in complex propagation environments [15, 16]. In this context, Multi-Input Multi-Output (MIMO) antenna systems [17] have emerged as a cornerstone technology, offering enhanced data throughput, link reliability, and spatial multiplexing capabilities.

However, achieving high gain and polarization diversity simultaneously remains a critical challenge in compact MIMO configurations [18]. Traditional approaches often involve

Fig. 1. The 2D ray-tracing formation of the lens antenna integrated with dual circularly polarized meta transmissive surface, $d_1 = 95$ mm, $d_2 = 34$ mm, $d_3 = 98$ mm, $h_1 = 7.3$ mm, $h_2 = 50$ mm, $h_3 = 15$ mm, $h_4 = 1$ mm, $l_f = 23.5$ P mm, $t_1 = 1.52$ mm, $t_2 = 1.52$ mm, $t_3 = 0.25$ mm, $t_4 = 2.43$, $t_4 = 2.25$, $t_5 = 2.25$, $t_6 = 2.25$, $t_7 = 2.25$.

trade-offs between gain, isolation, and polarization purity. To address these limitations, metasurfaces [19-21] have garnered significant attention due to their capacity to manipulate electromagnetic waves with subwavelength precision. In particular, lens formation incorporating with metatransmissive surfaces (MTS) provide an efficient platform for wavefront shaping and polarization control without significant radiation power loss.

This paper presents a high-gain MIMO lens antenna integrated with a dual circularly polarized meta-transmissive surface (DCP-MTS), specifically engineered for 6G applications. The proposed design incorporates an extended transition structure and a reflective wall to optimize wave focusing and prevention radiation leakage through the lateral openings. Moreover, the DCP-MTS enables left-handed circular polarization (LHCP) and right-handed circular

This work was supported by Institute of Information and Communications Technology Planning and Evaluation grant funded by the Ministry of Science and ICT, South Korea (RS-2019-III90008).

polarization (RHCP) conversion of dual-polarized incident waves along x- and y-axes [21], which are radiating by orthogonally oriented cross-dipole elements at the operating frequency $f_0 = 7$ GHz. The proposed MIMO-LA design demonstrate strong potential for 6G industrial applications, ensuring reliable performance across terrestrial [23, 24], airborne, and non-terrestrial networks.

II. DESIGN AND OPERATION

A. 2D Ray-tracing Model and Working Principle

The proposed MIMO-LA is shown in Fig. 1, which comprises of a 3D-printed lens with N varying dielectric constant layers, DCP-MTS, and dual linearly polarized dipoles as a radiator, which are placed at the bottom of the dipole's substrate with transmission lines on the top. Moreover, AMC is deployed under the dipole substrate at height h_1 to reflect back the dipole's radiation in the broadside direction with satisfies the constructive interference to enhance the realized gain. Also, reflective wall is employed to prevent the radiation leakage across the lateral openings. A gray resin with relative permittivity ($\varepsilon_r = 2.8$) and loss tangent $(\tan \delta = 0.05)$ is used to construct the 3D model of the MIMO-TL. A gray resin selection is based on its finest feature of 0.025 mm thickness of the constructed tier. A Taconic RF-35 substrate is used for the fabrication of the MTS and AMC, which has relative permittivity ($\varepsilon_r = 3.5$), loss tangent (tan $\delta =$ 0.0025) and thickness (1.52 mm) [20-22].

Fig. 1 also demonstrates the working principle of the MIMO-LA. It designed to enhance the broadside gain by ensure equal phase delay for diverse rays to obtained planar wavefront by

$$\beta_0 q_1 + \beta_{r1} l_1 = \beta_0 q_n + \beta_{rn} l_n \tag{1}$$

where $\beta_0=2\pi/\lambda_0$, $\beta_{rn}=2\pi\sqrt{\varepsilon_{rn}}/\lambda_0$ are the phase constants in air space and each tier of the dielectric lens, individually, q_1 is the focal length (l_j) , $l_1=h_2+h_3$. l_n is the phase delay for each distinct ray.

The geometries of the DCP-MTS and AMC unit cells are revealed in Fig. 2, while the dipole structure is illustrated in Fig. 3.

B. Meta Transmissive Surface (MTS) for Dual Circularly Polarization Converstion

The geometry of the DCP-MTS unit cell is depicted in Fig. 2a with normally incident plane waves aligned at a 45° polarization angle. To achieve circularly polarized (CP) transmission waves, two key conditions must be satisfied at the operating frequency $f_0=7$ GHz: (i) equal transmission magnitudes, such that $|S21_{dp1(x,x)}^{MTS}|=|S21_{dp1(y,x)}^{MTS}|$ and $|S21_{dp2(y,y)}^{MTS}|=|S21_{dp2(x,y)}^{MTS}|$, and (ii) a $\pm 90^\circ$ phase difference between orthogonal components, defined as $\Delta\phi=\phi_{dp1(x,x)}^{MTS}-\phi_{dp1(y,x)}^{MTS}$ and $\Delta\phi=\phi_{dp2(y,y)}^{MTS}-\phi_{dp1(x,y)}^{MTS}$. These conditions ensure the conversion of linearly polarized waves into left- or right-handed circularly polarized transmitted waves. The corresponding transmission magnitudes and phases are presented in Fig. 4.

C. Artificial Magnetic Conductor (AMC) as a Reflector

The AMC unit cell consist of metal square patch printed on a Taconic substrate, as illustrated in Fig. 2b. It is strategically place beneath the dipole substrate at an optimized

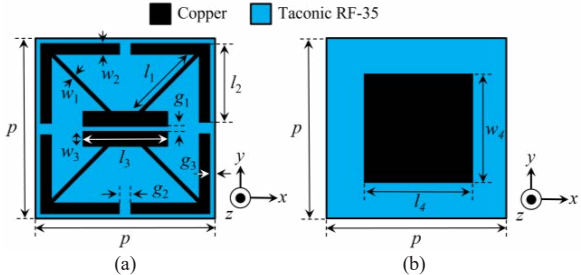


Fig. 2. The geometry of (a) the MTS unit cell, $l_1 = 4.9$ mm, $l_2 = 4.5$ mm, $l_3 = 3.7$ mm, $w_1 = 0.26$ mm, $w_2 = 0.49$ mm, $w_3 = 0.65$ mm, $g_1 = 0.55$ mm, $g_2 = 0.6$ mm, $g_3 = 0.2$ mm, p = 10 mm, (b) AMC unit cell, $l_4 = w_4 = 3$ mm, p = 10 mm

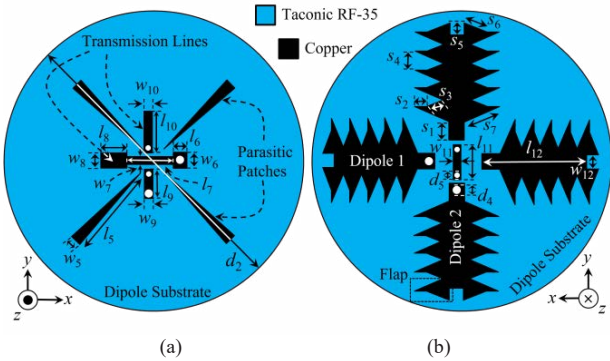


Fig. 3. The geometry of the radiator (a) top side, $l_5 = 9.52$ mm, $l_6 = 1.6$ mm, $l_7 = 3.51$ mm, $l_8 = 3.05$ mm, $l_9 = 2.77$ mm, $l_{10} = 5.28$ mm, $w_5 = 0.69$ mm, $w_6 = 1.6$ mm, $w_7 = 0.49$ mm, $w_8 = 1.6$ mm, $w_9 = 0.99$ mm, $w_{10} = 0.99$ mm, and (b) bottom side, $l_{11} = 2.49$ mm, $l_{12} = 13.1$ mm, $w_{11} = 0.5$ mm, $w_{12} = 0.99$ mm, $d_4 = 0.49$ mm, $d_5 = 0.5$ mm, $s_1 = 0.39$ mm, $s_2 = 1.6$ mm, $s_3 = 2.92$ mm, $s_4 = 2$ mm, $s_5 = 1.3$ mm, $s_6 = 3.45$ mm, $s_7 = 4.9$ mm.

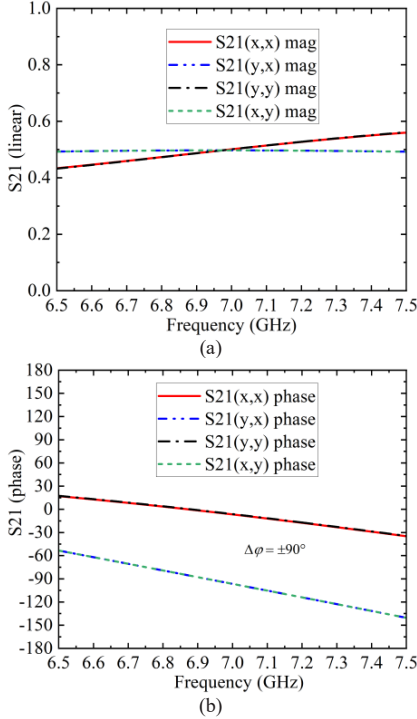


Fig. 4. The transmission characteristics of the meta transmissive surface (MTS): (a) magnitude, and (b) phase.

height h_1 to exhibit total reflection behavior. This configuration reflects the entire radiation from the dipoles back towards the $\pm z$ -axis, effectively enhancing forward

radiation. A wide phase response of the AMC is achieved for both x- and y-polarized incident waves by carefully designing the patch dimensions, where $l_4 = w_4$, and by selecting an appropriate periodicity p of the unit cell, The corresponding reflection magnitudes and phases are shown in Fig. 5.

D. Dual Cross-Dipoles as a radiator

The geometry of the dual x- and y-polarized cross-dipoles, employed as a dual-feeding structure, is illustrated in Fig. 3. These dipoles are excited using probe feeding with a diameter of d_3 . To enhance the radiation characteristics and miniaturize the copper-printed pattern, flaps are introduced on both sides of the dipoles. These flaps are etched on the other side of the dipole substrate, as revealed in Fig. 1. In addition, transmission lines are placed on the top side of the dipole substrate to achieve improved impedance matching. These transmission lines are connected through metallic vias with a wall thickness of 0.018 mm [21, 22] and a diameter of d_5 . To further reduce mutual coupling between the orthogonally placed cross-dipoles, parasitic patches are diagonally aligned and geometrically optimized, as illustrated in Fig. 3(a).

III. SIMULATION RESULTS

This section describes the performance evaluation of the proposed MIMO-LA, as shown in Figs. 6 and 7. The impedance bandwidths, represented by S11 and S22, are well maintained around the operating frequency $f_0 = 7$ GHz as illustrated in Fig. 6a. The simulated results reveal a -10 dB impedance bandwidth of approximately 480 MHz and 485 MHz for the two dipoles, respectively, corresponding to a fractional bandwidth of about 6.8 %. This indicates that the proposed MIMO-LA effectively covers the targeted 6G wireless communications band. Furthermore, the mutual coupling, represented by S21 and S12, between the two dipoles is suppressed to -35 dB at the operating frequency f_0 , supporting efficient MIMO performance.

Fig. 6b displays the co- and cross-polarized components of the realized gain. The peak realized gain are 13.58 dBi and 13.51 dBi for the respective dipoles. The 3dB gain bandwidths are 300 MHz and 290 MHz, leading to a bandwidth efficiency exceeding 62 %. Additionally, axial ratio (AR), also shown in Fig. 6b, demonstrates a 3dB AR bandwidth of 180 MHz for both dipoles, confirming the effective circular polarization performance.

The 2D radiation patterns of the MIMO-LA, illustrated in Fig. 7a for azimuth angles $phi = 0^{\circ}$ and 90° , show a sidelobe level (SLL) of -13.56 dB for both dipoles. This improvement is attributed to the use of the reflective wall as depicted in Fig. 1.

The key MIMO performance metrics —envelope correlation coefficient (ECC), diversity gain (DG), mean effective gain (MEG), and multiplexing efficiency (Mx. Eff.) — are extracted from the S-parameters and 3D radiation patterns, as defined by (2) to (5), and summarized in Fig. 7b. At the operating frequency f_0 , the ECC, DG, MEG, and Mx. Eff. are 0.00025, 9.99 dB, -3 dB, and -3.1 dB, respectively, validating the design's effectiveness for advanced MIMO applications.

$$ECC = \frac{|s_{11}s_{12}^* + s_{21}s_{22}^*|^2}{(1 - |s_{11}|^2 - |s_{21}|^2)(1 - |s_{22}|^2 - |s_{12}|^2)}$$
(2)

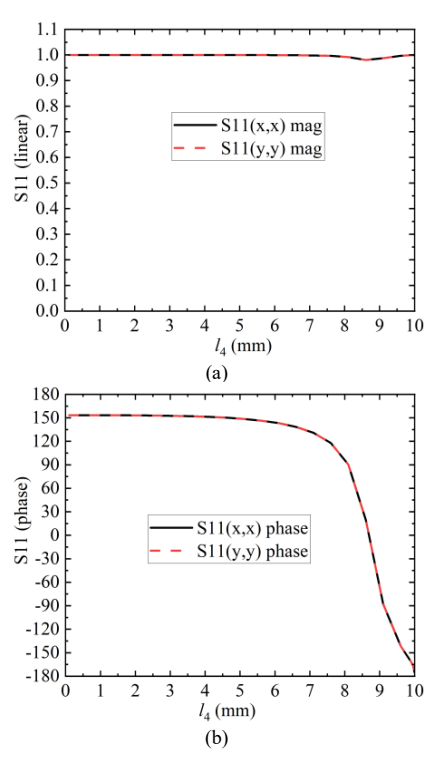


Fig. 5. The reflection characteristics of the artificial magnetic conductor (AMC): (a) magnitude, and (b) phase.

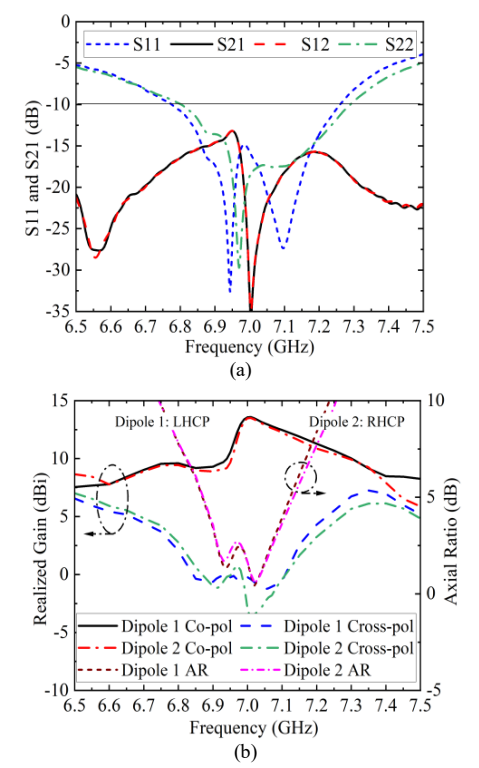


Fig. 6. The simulated results of MIMO lens: (a) The reflection coefficient, (b) peak realized gain and axial ratio.

$$DG = 10 \times log_{10}(1 - ECC) \tag{3}$$

$$MEG_n = \frac{1}{4\pi} \int_0^{2\pi} \int_0^{\pi} G_n(\theta, \phi) p(\theta, \phi) sin\theta d\theta d\phi \qquad (4)$$

$$Mx. \ Eff. = \sqrt{G_1.G_2}.(1 - |ECC|^2)$$
 (5)

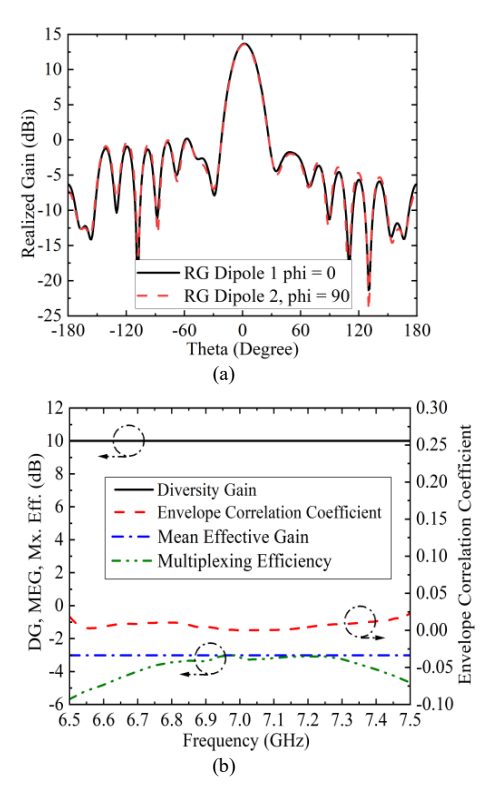


Fig. 7. The simulated results of MIMO lens: (a) 2D radiation pattern, and (b) diversity gain (DG), envelope correlation coefficient (ECC), mean effective gain (MEG), and multiplexing efficiency (Mx. Eff.).

The performance of the proposed MIMO lens antenna is compared with previously published circular polarized metasurfaces in Table I. The comparison shows that antenna achieves superior results in terms of realized gain, aperture efficiency, axial ratio (AR), and sidelobe level (SLL). These findings confirm that the MIMO lens antenna is highly effective in achieving a low AR while maintaining high realized gain and aperture efficiency in the broadside direction.

IV. CONCLUSION

In this study, we propose a MIMO-LA designed to enhance realized gain, impedance bandwidth, and improve the AR, ECC, DG, MEG, Mx. Eff., and aperture efficiency. The MIMO-LA employs dual-polarized dipoles backed by an AMC substrate and integrated with a lens and DCP-MTS to achieve high realized gain in the broadside direction for LHCP and RHCP. Additionally, a reflective wall structure is incorporated to suppress sidelobe levels and prevention of radiation leakage from the lateral openings.

As a result, the proposed antenna achieves a realized gain more than 13.5 dBi, an impedance bandwidth 480MHz, an SLL below –13.56 dB, a minimum AR 0.5 dB, and an aperture efficiency exceeding 50 %. Moreover, At the operating frequency f_0 , the ECC, DG, MEG, and Mx. Eff. are 0.00025, 9.99 dB, –3 dB, and –3.1 dB, respectively These performance characteristics demonstrate the suitability of the proposed MIMO-LA for a wide range of future 6G and next-generation wireless applications, including radar systems, advanced radio communication networks, microwave photonic filters (MWPF), and satellite communications, particularly in

TABLE I. COMPARISON OF THE PROPOSED MIMO LENS ANTENNA WITH PREVIOUSLY PUBLISHED CIRCULAR POLARIZED METASURFACES.

Comparison metrics	References			Proposed
	[25]	[26]	[27]	work
Operating frequency f_0	10.3	15	15	7
	GHz	GHz	GHz	GHz
Feeder	V-slot MPA ^a	MPA	AC- MPA ^b	Dual dipoles
Antenna type	FTA ^c	FTA	FPCA ^d	Lens antenna
Polarization	LHCPe	RHCP	LHCP / RHCP ^f	LHCP / RHCP
Realized Gain at f_0	21	24.9	19	13.8
	dBi	dBi	dBi	dBi
Aperture efficiency	18.5	17.1	14.8	50.8
	%	%	%	%
Axial ratio (AR) at f_0	0.4	0.5	0.6	0.45
	dB	dB	dB	dB
$SLL^{g} (phi = 0^{\circ})$ xz-plane	-13.1	-17.3	-8.0	-13.7
	dB	dB	dB	dB
SLL ($phi = 90^{\circ}$)	-14.5	-18.2	-8.2	-13.8
yz-plane	dB	dB	dB	dB

a. V-slot microstrip patch antenna, ^{b.} Aperture-coupled microstrip patch antenna, ^{c.} Folded transmittaray antenna, ^{d.} Fabry-Perot cavity antenna, ^{e.} Left-handed circular polarization, ^{f.} Right-handed circular polarization, ^{g.} Sidelobe level.

terrestrial, airborne, and non-terrestrial communications networks.

ACKNOWLEDGMENT

Jaeseong Kim is also affiliated with the School of Electrical Engineering, Korea University, 02841, Seoul, South Korea.

REFERENCES

- [1] S. Chen, S. Sun, and S. Kang, "System integration of terrestrial mobile communication and satellite communication—the trends, challenges and key technologies in B5G and 6G," *IEEE China Commun.*, vol. 17, no. 12, pp. 156-171, 2021.
- [2] C.-X. Wang, et. al., "On the road to 6G: Visions, Requirements, Key Technologies, and Testbeds," *IEEE Commun. Surv. & Tutor.*, vol. 25, no. 2, pp. 905-974, 2023.
- [3] N. P. Kuruvatti, M. A. Habibi, S. Partani, B. Han, A. Fellan, and H. D. Schotten, "Empowering 6G communication systems with digital twin technology: A comprehensive survey," *IEEE access*, vol. 10, pp. 112158-112186, 2022.
- [4] X. Chen, J. Tan, L. Kang, F. Tang, M. Zhao, and N. Kato, "Frequency selective surface toward 6G communication systems: A contemporary survey," *IEEE Commun. Surv. & Tutor.*, vol. 26, no. 3, pp. 1635-1675, 2024.
- [5] S. P. Dash, and A. Kaushik, "RIS-Assisted 6G Wireless Communications: A Novel Statistical Framework in the Presence of Direct Channel," *IEEE Commun. Lett.*, vol. 28, no. 3, pp. 717-721, 2024.
- [6] Q. Qi, X. Chen, A. Khalili, C. Zhong, Z. Zhang, and D. W. K. Ng, "Integrating Sensing, Computing, and Communication in 6G Wireless Networks: Design and Optimization," *IEEE Trans. Commun.*, vol. 70, no. 9, pp. 6212-6227, 2022.
- [7] A. V. Shvetsov, et. al., "Federated Learning Meets Intelligence Reflection Surface in Drones for Enabling 6G Networks: Challenges and Opportunities," *IEEE Access*, vol. 11, pp. 130860-130887, 2023.
- [8] Y. Xiao, et. al., "Space-Air-Ground Integrated Wireless Networks for 6G: Basics, Key Technologies, and Future Trends," *IEEE J. Sel. Areas Commun.*, vol. 42, no. 12, pp. 3327-3354, 2024.
- [9] C.-W. Chow, "Recent Advances and Future Perspectives in Optical Wireless Communication, Free Space Optical Communication and

- Sensing for 6G," *IEEE J. lightw. Technol.*, vol. 42, no. 11, pp. 3972-3980, 2024.
- [10] Y. H. Lou, Y. X. Zhu, G. F. Fan, W. Lei, W. Z. Lu, and X. C. Wang, "Design of Ku-Band flat Luneburg lens using ceramic 3-D printing," *IEEE Antennas Wireless Propag. Lett.*, vol. 20, no. 2, pp. 234-238, 2021
- [11] S. Lei, K. Han, X. Li, and G. Wei, "A design of broadband 3-D-printed circularly polarized spherical Luneburg lens antenna for X-Band," *IEEE Antennas Wireless Propag. Lett.*, vol. 20, no. 4, pp. 528-532, 2021.
- [12] G. Guo, Y. Xia, C. Wang, M. Nasir, and Q. Zhu, "Optimal radiation pattern of feed of Luneburg lens for high-gain application," *IEEE Trans. Antennas Propag.*, vol. 68, no. 12, pp. 8139-8143, 2020.
- [13] Y. Shi, K. Li, J. Wang, L. Li, and C. H. Liang, "An etched planar metasurface half Maxwell Fish-Eye lens antenna," *IEEE Trans. Antennas Propag.*, vol. 63, no. 8, pp. 3742-3747, 2015.
- [14] B. Fuchs, O. Lafond, S. Rondineau, M. Himdi, and L. L. Coq, "Off-axis performances of half Maxwell Fish-Eye lens antennas at 77 GHz," *IEEE Trans. Antennas Propag.*, vol. 55, no. 2, pp. 479-482, 2007.
- [15] M. Hussain, D. Kim, and K.-G. Lee, "Tapered Partially Reflective Surface Amplitude Distribution for High Gain and Low Side Lobe Level," *Proc. Conf. Korean Inst. Commun. Info. Sci. (KICS)*, Jeju, South Korea, Jun. 16-18, pp. 362-363, 2021.
- [16] M. Hussain, K.-G. Lee, and D. Kim, "Triangular Tapered Partially Reflective Surface Magnitude Distribution of Fabry-Perot Cavity for Peak Gain and Suppressed Sidelobes," Proc. Summer Conf. Korean Inst. Electromagn. Eng. Sci. (KIEES), Jeju, South Korea, Aug. 18-21, vol. 9, no. 1, 2021.
- [17] Z. Chen, C. N. Barati, J. Veihl, C. Shepard, and A. Sabharwal, "LensFD: Using Lenses for Improved Sub-6 GHz Massive MIMO Full-Duplex," *IEEE Trans. Veh. Technol.*, vol. 72, no. 6, pp. 7517-7529, 2023.
- [18] B. T. Malik, S. Khan, J. Nasir, and S. Koziel, "Enhanced Gain and Isolation Dual-Band Dual-Port MIMO Antenna With Integrated Lens

- for Millimeter-wave 5G Internet-of-Things Applications," *IEEE Access*, vol. 13, pp. 40859-40874, 2025.
- [19] Y. Wang, W. Zhang, Y. Chen, C.-X. Wang, and J. Sun, "Novel Multiple RIS-Assisted Communications for 6G Networks," *IEEE Commun. Lett.*, vol. 26, no. 6, pp. 1413-1417, 2022.
- [20] M. Hussain, K.-G. Lee, and D. Kim, "Tapered high-gain Fabry-Perot cavity antenna with high sidelobe suppression for 5G industry," Sci. Rep., vol.13, no. 1, p. 15744, 2023.
- [21] M. Hussain, K.-G. Lee, and D. Kim, "Circularly polarized high-gain Fabry-Perot cavity antenna with high sidelobe suppression," *Appl. Sci.*, vol. 13, no. 14, p. 8222, 2023.
- [22] M. Hussain, K.-G. Lee, and D. Kim, "Circular Polarized Resonance Cavity Antenna for Peak Gain and Suppressed Sidelobes," Proc. Summer Conf. Korean Inst. Electromagn. Eng. Sci. (KIEES), Jeju, South Korea, Aug. 17-20, vol. 10, no. 1, 2022.
- [23] M. Song, H. Choi, Y. Jung, T. Lee, G. Choi, J. Lee, and M. Song, "Multiband microwave photonic filters with tunability and programmability via optical frequency comb shaping," *J. Lightw. Technol.*, vol. 41, no. 23, pp. 7215-7222, 2023.
- [24] M. Hussain, Y. Amin, and K.-G. Lee, "A Compact and Flexible UHF RFID Tag Antenna for Massive IoT Devices in 5G System," Sensors, vol. 20, no. 19, p. 5713, 2020.
- [25] J. Yang, S. T. Chen, M. Chen, J. C. Ke, M. Z. Chen, C. Zhang, R. Yang, X. Li, Q. Cheng, and T. J. Cui, "Folded transmitarray antenna with circular polarization based on metasurface," *IEEE Trans. Antennas Propag.*, vol. 69, no. 2, pp. 806-814, 2020.
- [26] H. Lei, Y. Liu, Y. Jia, Z. Yue, and X. Wang, "A Low-Profile Dual-Band Dual-Circularly Polarized Folded Transmitarray Antenna With Independent Beam Control," *IEEE Trans. Antennas Propag.*, vol. 70, no. 5, pp. 3852-3857, 2021.
- [27] J. Li, and X. Huang, "Dual Circular Polarization Fabry–Perot Resonant Antennas Based on Meta-Surface," *Electronics*, vol. 12, no. 1, p. 173, 2022.